Hot-carrier dynamics in mesoscopic structures

1992 Semicond. Sci. Technol. 7 B202

(http://iopscience.iop.org/0268-1242/7/3B/050)

Semicond. Sci. Technol. 7 (1992) B202–B209. Printed in the UK

Hot-carrier dynamics in mesoscopic structures

J P Leburton and D Jovanovic

Beckman Institute for Advanced Science and Technology, and Coordinated Science Laboratory, University of Illinois at Urbana-Champaign, Urbana, IL61801, USA

Abstract. We discuss a wide variety of new phenomena caused by high levels of confinement in mesoscopic systems, which affects the dynamics and statistical distribution of the carriers. A simulation of the low-temperature transport in quantum wires shows the onset of velocity oscillations arising from optical phonon emission in moderate electric fields. At high temperatures, transport nonlinearities are manifested by high carrier mobility and substantial carrier cooling. Pronounced resonances between the optical-phonon energy and the subband separation give rise to population inversion between adjacent off-resonance subbands induced by 'phonon pumping'. Under high-field conditions carriers rapidly escape from quantum wires through intervalley scattering and real space transfer.

1. Introduction

In the last several years low-dimensional systems have been the subject of intense investigation (for a review see, for example, [1]). Mesoscopic structures such as quantum rings and wires have been purposely designed to show a wide variety of new phenomena ranging from universal conductance fluctuations [2, 3] and quantum interferences [4–7] to the Aharanov–Bohm effect [8, 9]. Quantum wire-based lasers have been fabricated using novel techniques for achieving transverse confinement by direct growth on vicinal GaAs substrates [10, 11]. Meanwhile, the observation of Shubnikov–de-Haas-type oscillations in the transconductance of an array of electrostatically confined quantum wires has confirmed the existence of one-dimensional (1D) quantized subbands above the liquid nitrogen temperature [12]. These discoveries have fostered technological initiatives for the applications of mesoscale phenomena in new forms of high-performance electronic and optical devices. Normal device operation, however, requires a room temperature environment and voltage biases significantly higher than those needed to observe quantum interference phenomena. While transverse quantization can be maintained over a wide temperature range, it is doubtful that the long-range phase-coherence causing quantum interference effects can be preserved in the presence of the inherent dissipative mechanisms; a particle picture for transport appears more realistic [13].

Small structure size and confinement have dramatic effects on the lattice dynamics as well as on electronic processes. For instance, in structurally confined systems, the spectrum of optical phonons is no longer continuous, and it splits in confined bulk modes and surface modes with numerous influences on carrier relaxation [14]. In quantum wires the reduction of momentum space to a single dimension (even with multiple transverse modes) results in singularities in the carrier density of states (DOS) and modifies the nature of particle collisions by limiting the number of final scattering states; a significant enhancement of the 1D carrier mobility compared with bulk and two-dimensional systems has been predicted [15, 17]. Also, the statistical energy distribution of carriers is quite sensitive to disturbances from equilibrium quite and acquires non-linear components [18]. These new findings anticipate a rich field of novel effects. In this paper we focus on transport in systems with double confinement, or quantum wires.

2. Electronic model

There are several ways to achieve double-particle confinement and realize quantum wire structures. They range from high structural confinement between layers of wide-gap materials (figure 1(*a*)) [11, 15] to a combination of electrostatic and structural confinement at the interface of material with different band gaps (figure 1(*b*)) [12, 19]. In this analysis we assume simple confinement configurations arise from the elementary GaAs–AlGaAs potential wells, which are decoupled along the two transverse directions, y and z. Electrons are free to move longitudinally in the x-direction with their energies and wavefunctions given by

$$E_{ij}(k_x) = \frac{\hbar^2 k_x^2}{2m^*} + E_i + E_j, \quad i,j = 1, \ldots, N, \tag{1}$$

and

$$\psi_{ij}(k_x, \boldsymbol{r}) = \frac{1}{\sqrt{L_x}} e^{ik_x x} \xi_i(y)\phi_j(z) \tag{2}$$

0268-1242/92/03B202 + 08 $04.50

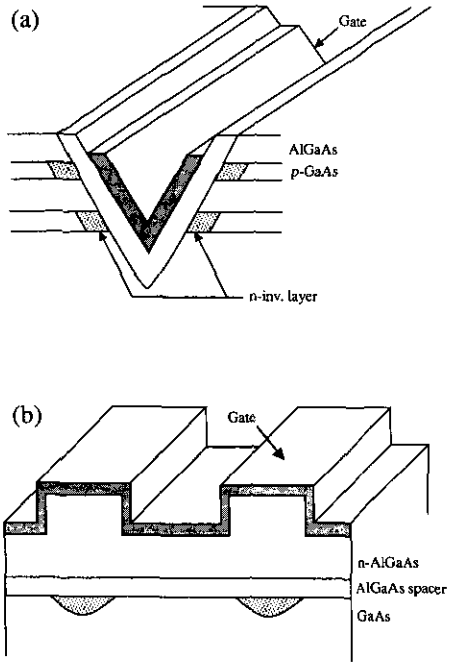

Figure 1. (*a*) Schematic cross section of a quasi-1D structure fabricated by the anisotropic etching of a V-shaped groove into a multiple-well heterostructure (V-FET) (after Sakaki, [15]) and (*b*) a MODFET-based structure with a grating etched into the AlGaAs cap layer (G-FET) (after Ismail *et al* [12]).

where k_x and L_x are the wave vector and the wire length in the longitudinal direction and $\xi_i(y)$ and $\phi_j(z)$ are the transverse wavefunctions that correspond to the quantized energy levels E_i and E_j, respectively. N is the maximum number of levels considered in a particular confinement situation. The remaining term in equation (1) is the kinetic energy of the particle resulting from the free-electron component of the overall electronic wavefunction (equation (2)). The advantage of dealing with elementary configurations is the decoupling of the electronic *y*- and *z*-wavefunctions, which facilitates the computation of the scattering rates.

3. Scattering rates

Several scattering mechanisms play a minor role in the carrier relaxation and the response times in quasi-1D systems. For instance, impurity scattering is insignificant in contemporary modulation-doped GaAs structures, especially under high-field conditions [15, 20]. In addition, electron-electron (e–e) scattering vanishes for 1D intrasubband transitions since indistinguishable particles simply exchange energy and momenta during binary collisions [16]. For intersubband transitions, however, e–e scattering is expected to contribute to the scattering background, but owing to the large momentum exchanges, this coupling is weak and can therefore be neglected in most analyses. As a result, the large-scale transport properties of quasi-1D III–V systems are primarily determined by deformation potential acoustic and optical scattering and by polar optical-phonon scattering.

In the semiclassical limit the expression for the transition probability, $S_{vv'}(k_x, k'_x, q)$, is

$$S_{vv'}(k_x, k'_x, q) = \frac{2\pi}{\hbar}|M_{vv'}(k_x, k'_x, q)|^2\delta[E_{v'}(k'_x) - E_v(k_x) \pm \hbar\omega_q]. \tag{3}$$

Here, $M_{vv'}(k_x, k'_x, q)$ represents the electron–phonon matrix element for a transition from the initial k_x, v state to the final k'_x, v' state mediated by a phonon with wavevector q. The $\pm$ sign in the energy-conserving δ-function accounts for the emission (+) and absorption (−) of phonons between the subbands with indices $v(i,j)$ and $v'(i',j')$. The total scattering rate from an initial state with energy E is therefore given by

$$\frac{1}{\tau_v(E)} = \frac{A}{(2\pi)^2}\sum_{v',k'_x}\int dq_\perp S_{vv'}(k_x, k'_x, q), \tag{4}$$

where A is the wire cross section and the summation over the final k'_x, v' states takes into account all the possible intersubband transitions along with those occurring within the same band, v. The integral over the transverse phonon wave vectors, $q_\perp$, sums over all the phonons that give rise to a particular final k'_x state.

At room temperature, the polar optical-phonon (POP) mechanism is the dominant scattering mechanism for carrier energies $E \leqslant 0.3$ eV. In conditions of structural confinement the presence of heterointerfaces introduces discontinuities in the material dielectric constants that modify the nature of the lattice dynamics; longitudinal optical (LO) modes become confined while new surface optical (SO) modes appear. The electron–phonon scattering rate is, therefore, affected by this change in the lattice dynamics as has recently been pointed out by Stroscio *et al* [14]. Figure 2(*a*) shows the scattering rates for different optical modes in square quantum wires of size $d = 40$ Å at $T = 300$ K, for two confinement conditions (i) a GaAs wire embedded in AlAs material and (ii) a GaAs wire standing in atmospheric-pressure air. In both cases it is seen that the SO modes make significant contributions to the total scattering rate especially in the case of free-standing wires where the SO rate exceeds the LO emission rate [21]; notice the divergence in the rates which is due to the 1D DOS. In relaxing the confinement, the influence of the interface decreases, and so do the SO rates, which become negligible for $d \geqslant 100$ Å. In the case of electrostatic confinement represented in figure 1(*b*), only carriers are confined and extended bulk LO modes are the dominant optical-phonon scattering mechanism. The $1/\sqrt{E}$ divergence in the LO rates persists as a consequence of the semiclassical formulation of the Fermi golden rule.

A more accurate description of the electron–phonon interaction considers the self-energy of the polaron, $\Sigma(k_x, E)$. The latter can be evaluated in the Fock approxi-

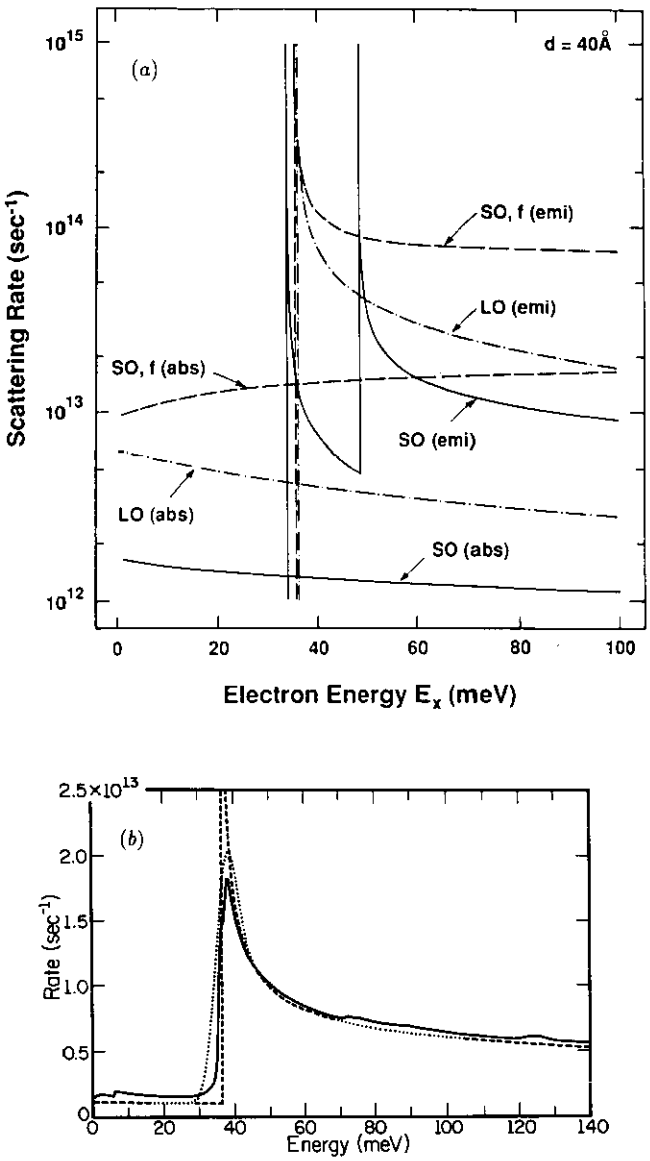

Figure 2. (*a*) Scattering rates for square quantum wires of size $d(=L_z=L_y) = 40$ Å as a function of longitudinal energy at $T = 300$ K. Here SO, f and SO stand for the SO modes in free standing wires and in GaAs/AlAs wires, respectively; LO denotes the confined POP modes while emi (abs) denotes phonon emission (absorption), (after Kim *et al* [21]. (*b*) Comparison of POP scattering rates computed by the Fock approximation (full curve), the Fermi golden rule using the classical unbroadened density of states (broken curve) and the Fermi golden rule using the classical density of states convolved with a Gaussian broadening function fitted to the Fock result (dotted curve). The broadening of the fitted curve is conveyed by a constant broadening factor, $\Gamma = 2.5$ meV at 300 K.

mation, which after being adapted to the quasi-1D problem, [22], gives

$$\Sigma(k_x, E) = \int \frac{dq_x}{2\pi} \frac{g^2_+(k_x - q_x)}{E - \hbar\omega_q - \varepsilon(q_x) - \Sigma(q_x, E - \hbar\omega_q)} + \int \frac{dq_x}{2\pi} \frac{g^2_-(k_x - q_x)}{E + \hbar\omega_q - \varepsilon(q_x) - \Sigma(q_x, E + \hbar\omega_q)} \tag{5}$$

with

$$g^2_\pm(k_x - q_x) \equiv \frac{1}{4\pi^2} \int dq_y\, dq_z |(k'_k v'|V_q e^{\pm iq\cdot r}|k_x, v)|^2. \tag{6}$$

Here V_q is the electron–phonon coupling factor.

Even though equation (5) treats the issue of collision broadening in much more detail than the Fermi golden rule, it has its own shortcomings in that it yields an incorrect binding energy for the 1D polaron and does not include the overall lowering of the subband energies owing to the transverse phonon component. In addition, equation (5) is computationally cumbersome owing to its self-consistent nature, and is further complicated by the introduction of the round-off errors resulting from divergences in the denominator for the quasi-1D dispersion, $\varepsilon(q_x)$. A solution by Briggs *et al* for the POP interaction (figure 2(*b*)) demonstrates a substantial broadening in the emission peak, which plays an important role in scattering processes at high temperatures [22]. For practical purposes, the golden-rule formalism can be retained by convolving a Gaussian broadening function containing a constant broadening factor, Γ, with the bare 1D density of states so that [23]

$$D(E) = \frac{1}{2\hbar\Gamma}\left(\frac{m}{\pi}\right)^{1/2} \int_{-E}^{\infty} e^{-E'^2/2\Gamma^2} \frac{1}{(E' + E)^{1/2}} dE'. \tag{7}$$

This method, with a proper choice of Γ, gives a good representation of the quantum corrections to the scattering rates (figure 2(*b*)) and substantiates, using the golden rule with equation (7), the replacement of the classical density of states.

4. One-dimensional transport phenomena

We study transport phenomena in quasi-1D systems at both low and high temperatures with a Monte Carlo simulation that has been described elsewhere [13]. Low-temperature transport ($T \leqslant 77$ K) is characterized by the absence of LO phonon absorption, an electronic distribution that occupies only the bottom few subbands, and an evolution of the distribution that exhibits spatially dependent velocity oscillations. The contribution of phonon absorption at higher temperatures is predicted to lead to other phenomena such as anomalous carrier cooling, resonant intersubband optical-phonon scattering (RISOPS), intersubband population inversions and escape mechanisms similar to real-space transfer.

4.1. Low-temperature transport

A spatially dependent Monte Carlo code was used to study the carrier evolution from an initial Maxwell–Boltzmann distribution under the sudden application of a longitudinal electric field F_x at low temperatures. This situation is analogous to the injection of carriers from a bulk region (source) at thermal equilibrium, into a quasi-1D channel. The low rate of phonon absorption implies

that carrier transport will be essentially ballistic in the active region up to the POP emission threshold, at which point carriers will emit a phonon and lose energy. This process is repeated for several periods until spatial dephasing and randomization by acoustic phonon scattering causes the electrons to converge onto a steady-state quasi-1D distribution. Figure 3 shows the carrier velocity at 77 K with a longitudinal field $F_x = 100\,\mathrm{V\,cm^{-1}}$. The non-zero initial velocity reflects the forward component of the initial Maxwell–Boltzmann velocity distribution since these are the only carriers that are injected into the active region. As the electrons drift under the influence of the field they overshoot their steady state velocity several times in a manner analogous to an underdamped oscillator. The period of oscillation, x_c, can be derived classically by recognizing that quasi-ballistic transport occurs only for energies below the POP energy, $\hbar\omega_{pop}$, so that

$$x_c = \hbar\omega_{pop}/eF_x \tag{8}$$

For $F_x = 100\,\mathrm{V\,cm^{-1}}$, $x_c = 3.6\,\mu\mathrm{m}$, which correlates well with the data in figure 3. This effect is similar to the velocity overshoot effect observed in short-channel MOSFET in that the initial distribution is accelerated by the field causing the electron temperature to exceed the lattice temperature. In quasi-1D channels this type of behaviour persists over several periods owing to the absence of angular randomization and the high peaks in the POP emission rates which permit relaxation to the subband minima in a quasi-coherent manner. The effect occurs for an intermediate range of F_x because at low fields the transport properties are dominated by acoustic phonon scattering which causes a randomization of the carrier distribution. Under high-field conditions the spatial coherence of the electron–phonon dynamics is destroyed by high-energy intersubband scattering. A similar effect has been predicted for bulk semiconductors although with a weaker intensity owing to angular randomization and inherent background impurity scattering [24, 25]. We believe that quantum wires would be ideal for observing this oscillatory behaviour in a modulation-doped configuration.

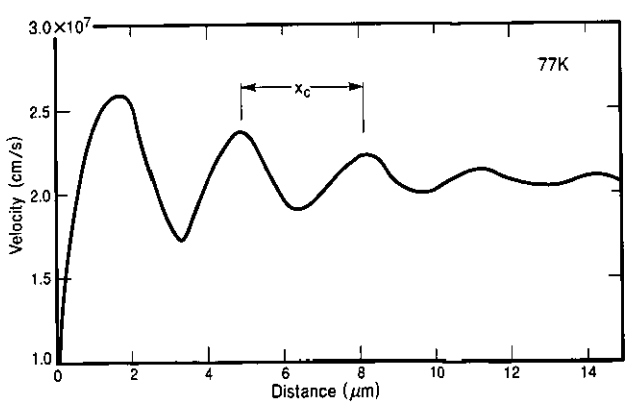

Figure 3. Electron velocity plotted against distance in a quasi-1D channel at 77 K with $F_x = 100\,\mathrm{V\,cm^{-1}}$. The initial velocity represents the average forward velocity of the initial distribution (Maxwell–Boltzmann).

4.2. High-temperature transport

At high temperatures ($T > 77$ K), because of the absence of angular scattering, the electronic distribution already shows significant deviations from the Maxwellian distribution in the low range of intermediate fields.

4.2.1. Carrier cooling and enhanced mobility. Figure 4 shows the profile of the energy distribution $f(E)$ for $F_x = 100\,\mathrm{V\,cm^{-1}}$ at $T = 300$ K compared with an approximate solution of the Boltzmann equation for POP scattering only, inclusion of acoustic phonon scattering does not modify significantly these results. The quantum wire structure considered here consists of the QW of figure 1(*a*) with $L_y = 135$ Å and a triangular potential with $F_z = 120\,\mathrm{kV\,cm^{-1}}$. These high-confinement conditions put the ground level at 138 meV above the GaAs band gap, and make the occupation of the upper subband practically negligible. The structures observed in $f(E)$ are a direct consequence of the singularities in the 1D density of states and the emission and absorption of phonons with constant energy, $\hbar\omega_{POP}$, which favour energy occupation at $E = n\hbar\omega_{POP}$. The agreement between the numerical and analytical results is very good except near $E = n\hbar_{POP}$ where the discrepancy arises from quantum broadening in the density of states, which is accounted for in the Monte Carlo model (see section 3). The structures in $f(E)$ manifest an organization in k-space that arises from the disturbance of the Maxwellian equilibrium by the longitudinal electric field. This onset of order in $f(E)$ is related to an important thermodynamic effect, the cooling of the carriers below their thermal energy $kT/2$. The inset in figure 4 shows that for $F_x < 50\,\mathrm{V\,cm^{-1}}$ the distribution is

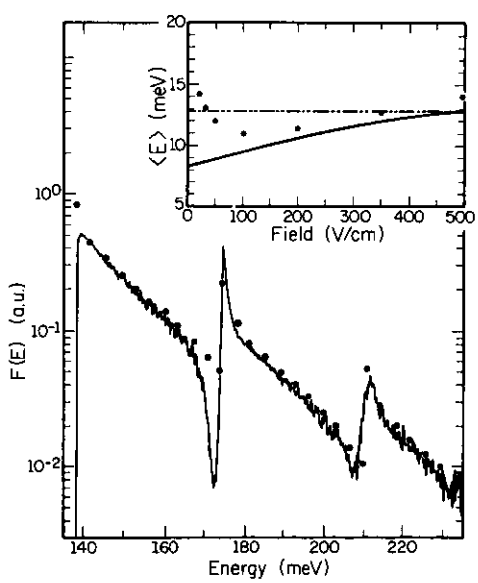

Figure 4. Energy distribution functions of a single-band quasi-1D electron gas with $F_x = 100\,\mathrm{V\,cm^{-1}}$ at $T = 300$ K. Both Monte Carlo (full curve) and analytical (dots) results are plotted. The inset shows the average carrier energy as a function of F_x for Monte Carlo (dots) and analytical (full curve) models. The average thermal energy, $kT/2$, is also shown (chain curve).

heated up owing to acoustic-phonon (AP) scattering, but above 50 $V\,cm^{-1}$, the influence of AP decreases rapidly and POP become the dominant scattering mechanism, characterized by a minimum in the average energy $\langle E \rangle$ around $F_x = 100\,V\,cm^{-1}$. This minimum in $\langle E \rangle$ corresponds to the onset of structures and organization in $f(E)$. Increasing electric fields tends to compete with the POP-induced organization and increase the average carrier energy. As seen in the inset of figure 4, the analytical solution of the Boltzmann equation follows the same trend as the Monte Carlo simulation, except at low fields where AP scattering and other randomizing mechanisms have been neglected, and therefore shows a lower average energy. The decrease in $\langle E \rangle$ below lattice temperature is associated with a mobility enhancement which, at $100\,V\,cm^{-1}$, can be as high as $3 \times 10^4\,cm^2\,V^{-1}\,s^{-1}$ and thus is much larger than the bulk value [16]. Thus the onset of structures and carrier cooling are a consequence of 1D forward absorption of constant POP whereby under non-equilibrium high-temperature conditions, thermal energy is converted in drift motion to enhance the transport response. We would like to point out that the absence of intrasubband (binary) electron–electron collisions limits the thermalization and provides grounds for the validity of our model.

The velocity–field relation is shown in figure 5(*a*), along with the equivalent relation for bulk GaAs. The velocity at $F_x = 500\,V\,cm^{-1}$ corresponds to a mobility of $16160\,cm^2\,V^{-1}\,s^{-1}$, which is still twice the bulk value of

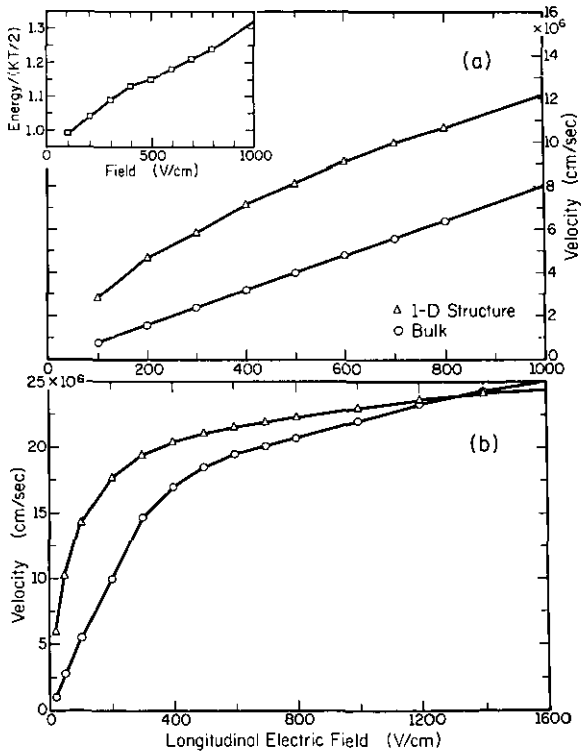

Figure 5. Velocity–field relation for a V-FET ($L_y = 135$ Å and $F_z = 120\,kV\,cm^{-1}$) compared with bulk GaAs at (a) 300 K and (b) 77 K. The inset shows the average electron energy, in units of kT, as a function of the longitudinal field.

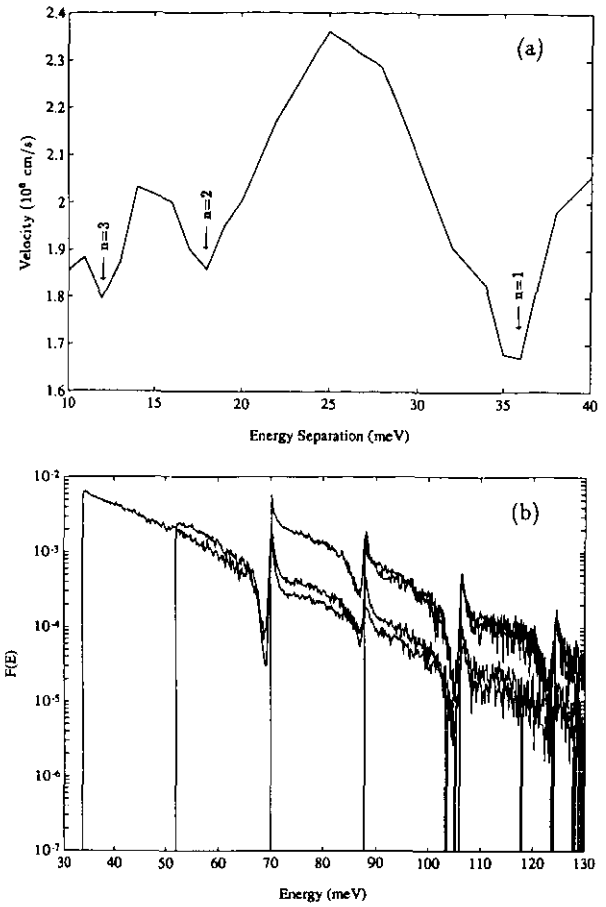

Figure 6. (*a*) Electron velocity as a function of subband energy separation at $T = 150$ K. The data are taken for a system with $L_y = 150$ Å and $F_x = 100\,V\,cm^{-1}$. The occurrence and order, n, of RISOPS are indicated by the arrows. (*b*) Distribution functions for a second-order resonant system with the same confinement as in (*a*). Each curve represents the relative distribution of a particular subband with the energy origin lying at the Γ-valley minimum. Population inversion occurs between the third (resonant) subband and the second.

$8000\,cm^2\,V^{-1}\,s^{-1}$ [23]. The differential mobility at low fields is over three times as large as the bulk value and converges towards the latter at higher fields as electrons heat up and scatter to the upper subbands. The velocity–field curve for the same confinement conditions at 77 K is shown in figure 5(*b*). At low fields the differential mobility is higher in the 1D system than in the bulk, while at high fields the velocities again approach the same value.

The $f(E)$ structures visible at multiples of the POP energy in figure 4 are relatively robust and persist under lower confinement, where the basic features of this effect contribute to enhanced POP-assisted intersubband resonances and the onset of population inversion (see section 4.2.3).

4.2.2. Resonant intersubband optical-phonon scattering. Two subbands are defined to be in resonance when the spacing between them approaches the POP energy $\hbar\omega_{POP}$. Of specific interest is high-order resonant intersubband optical-phonon scattering (RISOPS) for

which one or more non-resonant subbands lie between two bands in the resonance [26, 18]. As the spectrum of 1D subbands is passed through RISOPS, velocity oscillations similar to the longitudinal magnetophonon effect occur over a wide range of temperatures. Single-carrier multisubband Monte Carlo simulation of a GaAs–AlGaAs structure shows velocity fluctuations as a function of confinement (figure 6(*a*)). This effect, which is modelled here for a quantum wire consisting of an infinite quantum well and an electrostatic parabolic potential, appears to be optimum at $T = 150\,\mathrm{K}$ since there is a trade-off between a significant POP absorption rate and small collision broadening [27]. Velocity minima occur during RISOPS, that is $n\Delta E = \hbar\omega_{\mathrm{POP}}$ (n is an integer and ΔE a constant energy separation of the harmonic oscillator) for which the intersubband POP scattering rate is a maximum owing to the peak in the joint 1D density of the states of the two interacting subbands.

4.2.3. Intersubband population inversion. Another interesting feature in $f(E)$ is the occurrence of intersubband population inversion under RISOPS conditions with the potential for far-infrared (FIR) stimulated emission [28]. Population inversion is found to occur for the second-order resonant configuration, at $T = 150\,\mathrm{K}$, between the third and second subbands with relative occupancies, O_{rel}, of 19.9 and 19.4%, respectively (figure 6(*b*)). For a third-order resonance configuration, we found $O_{\mathrm{rel}} = 14.0\%$ for the fourth subband and $O_{\mathrm{rel}} = 11.8\%$ for the third subband. It should be noted that although population inversions exist between harmonic oscillator subbands, they tend to be weaker than in quantum wires with irregularly spaced subbands. This is due to the propagation of RISOPS to the upper equally spaced harmonic oscillator subbands. As a result the carrier population tends to be more dispersed in energy, thereby smoothing out any distribution anomalies. This is particularly noticeable at room temperature, where population inversion does not occur because the high absorption rate transfers electrons to the upper subbands very effectively.

In the quantum wires realized with a triangular potential $eF_z z$ and a quantum well of width L_y, the unequally spaced energy levels lead to two possible configurations

(*a*) $F_z = 23\,\mathrm{kV\,cm^{-1}}$ and $L_y = 215\,\text{Å}$, which places the first excited y-state ($n_y = 2, n_z = 1$) in resonance with the ground state ($n_y = 1, n_z = 1$), and the first excited z-state ($n_y = 1, n_z = 2$) just below the excited y-state (figure 7(*a*)).

(b) $F_z = 10\,\mathrm{kV\,cm^{-1}}$ and $L_y = 150\,\text{Å}$ for which the second excited z-state ($n_y = 1, n_z = 3$) is in resonance with the ground state, and the first excited z-state ($n_y = 1, n_z = 2$) is the intermediate level (figure 7(*b*)).

Stimulated emission is only possible in the latter case because the optical transition ($n_y = 2$, $n_z = 1 \rightarrow n_y = 1$, $n_z = 2$) in case (a) is forbidden owing to the selection rules between independent y- and z-states. In case (b), Monte Carlo simulation for a longitudinal field $F = 200\,\mathrm{V\,cm^{-1}}$ shows that 24% of the carriers are in the upper band at $T = 300\,\mathrm{K}$ with only 4% in the intermediate subband.

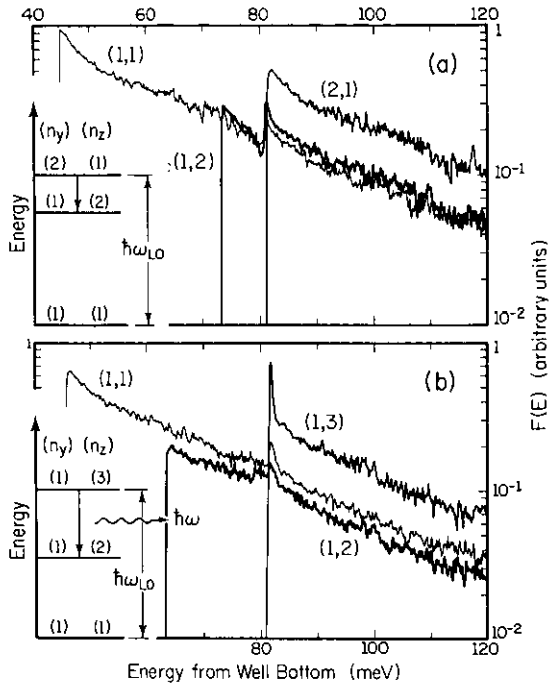

Figure 7. Distribution functions showing population inversion between (a) the (2, 1) and (1, 2) bands and (b) the (1, 3) and (1, 2) bands. The insets show the energy level diagrams under RISOPS conditions along with possible optical transitions. Because of selection rules in the optical matrix element, transitions between subbands cannot occur when both the y- and z-quantum numbers change (case (a)).

In order to assess the possibility for stimulated emission between inverted subbands, the theoretical gain given [29] by

$$g(\omega) = \frac{\Delta N}{A}\frac{e^2}{\bar{n}\varepsilon_0 c E_{ij}\hbar_2}|\langle j|\boldsymbol{e}\cdot\boldsymbol{r}|i\rangle|^2\frac{T_2}{1+(\omega-\omega_{ij})^2T_2^2} \qquad (9)$$

has been calculated to be about $900\,\mathrm{cm^{-1}}$ at its peak value, for a population difference $\Delta N = 4\times10^5\,\mathrm{cm^{-1}}$, a wire cross section $A = 5\times10^{-12}\,\mathrm{cm^2}$, and an energy separation $E_{ij} = \hbar\omega_{ij} = 18\,\mathrm{meV}$. Here, $\boldsymbol{e}$ is the optical polarization vector and we have assumed the intersubband scattering time to be $T_2 = 10^{-13}\,\mathrm{s}$. The substantial value of the gain is encouraging and should make FIR stimulated emission observable in highly packed 1D structures. In this respect the novel techniques of quantum wire fabrication by direct growth on patterned vicinal substrates [30] offer promising opportunities to realize FIR lasers operating by 'phonon pumping' in quantum wire structures†.

4.2.4. Intervalley scattering and carrier escape. A serious issue affecting the carrier dynamics is electron emission from the quantum wire at sufficiently high electric fields;

† We would like to emphasize that POP scattering is actually the pumping mechanism that creates population inversion here, while in other configurations such as tunnelling injection in superlattices, it is the principal limitation on the quantum efficiency.

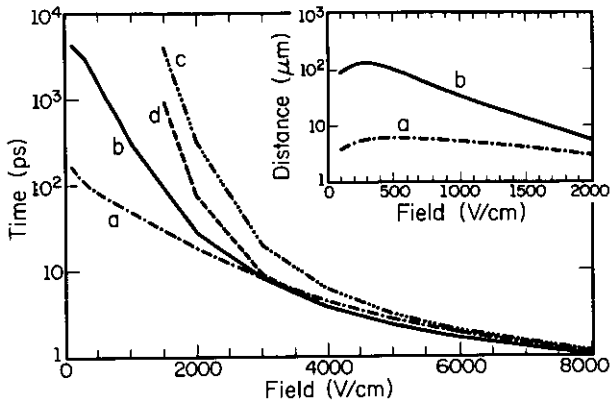

Figure 8. Electron lifetime plotted against longitudinal field at 77 and 300 K for high- and low-confinement conditions. Here a and b are the high- and low-confinement curves at 300 K, respectively, while c and d are the corresponding curves at 77 K. The inset shows the escape distance plotted against the longitudinal field.

the carriers gain enough energy from the field to overcome the confining barrier [31]. The escape mechanisms depend on the wire configuration and include real space transfer effects such as emission from a quantum well, or carriers drifting away from a heterojunction. Carrier losses due to scattering include intravalley as well as intervalley phonon scattering to 3D states. If the losses from these mechanisms are significant, either in terms of electron lifetimes or the mean paths in the wire, then the whole concept of an infinitely long, semiclassical quantum wire is invalid.

The influence of the longitudinal field on the lifetime is calculated by Monte Carlo techniques and is shown in figure 8 for high- and low-confinement conditions at both 77 and 300 K; curve a (b) is for high (low) confinement at 300 K while curve c (d) is high (low) confinement at 77 K. In the high-confinement cases, we have assumed that the initial electron energy is 140 meV, while in the low-confinement cases the initial electron energy is 50 meV. Varying the initial energy does not substantially alter the results except for cases with very high initial energies. All the curves show a very strong dependence on the longitudinal field. At low fields the effects of confinement and temperature are significant, but at higher fields these effects disappear and only the field is relevant in determining the lifetime. The escape times (for the same field) are larger at 77 K because of the lack of phonon absorption, which tends to both lower the average energy and also raise the threshold for intervalley scattering. The 77 K data do not go below 1500 V cm^{-1} because the lifetime is over 10 ns.

The high-confinement condition at 300 K shows a much shorter lifetime than the low-confinement case. This is due to the fact that under high confinement the average energy is high because of the location of the bottom subband relative to the L and X valleys. However, at 77 K the trend is reversed and under low confinement a large fraction of carriers is above the emission threshold. The inset in figure 8 shows an estimate of the distance an electron travels for (a) high and (b) low confinement at 300 K. The distance in the low-confinement case is much larger than that for the high-confinement case, even though the electron velocities in the high-confinement case are larger than in the low-confinement case. The distance rises rapidly, peaks near 400 V cm^{-1}, and then falls off slowly.

The escape of carriers from quantum wires is a fundamental effect that can either be exploited or avoided by proper design of the 1D structure. With the aid of Monte Carlo simulation we have obtained both the length and time scales that establish the range of validity for treating the system as a closed 1D electron gas.

Acknowledgments

The authors would like to thank Dr Stephen Briggs for laying much of the foundation of this work. This work was supported by JSEP under grant no N00014-90-J-1270. All of the computations were performed using the resources of the National Center for Supercomputing Applications (NCSA) and the National Center for Computational Electronics (NCCE) at the University of Illinois.

References

[1] Reed M A and Smith W P (eds) 1990 *Nanostructure Physics and Fabrication* (Boston: Academic)
[2] Skocpol W J, Jackel L D, Hu E L, Howard R E and Fetter L A 1982 *Phys. Rev. Lett.* **49** 951
[3] Wheeler R G, Choi K K, Goel A, Wisnieff R and Prober D E 1982 *Phys. Rev. Lett.* **49** 1674
[4] Timp G, Chang A M, Mankiewich P, Behringer R, Cunningham J E, Chang T Y and Howard R E 1987 *Phys. Rev. Lett.* **59** 732
[5] van Wees B F, van Houten H, Beenakker C W J, Williamson J G, Kouwenhoven L K, van der Marel D and Foxon C T 1988 *Phys. Rev. Lett.* **60** 848
[6] Roukes M, Scherer A, Allen S, Craighead H, Ruthen R, Beebe E and Harbison J 1987 *Phys. Rev. Lett.* **59** 3011
[7] Ford C J B, Thornton T J, Newbury R, Pepper M, Ahmed H, Peacock D C, Ritchie D A, Frost J E F and Jones G A C 1988 *Phys. Rev.* B **38** 8518
[8] Datta S, Melloch M R, Bandyopadhyay S, Noren R, Vaziri M, Miller M and Reifenberger R 1985 *Phys. Rev. Lett.* **55** 2344
[9] Washburn S and Webb R A 1986 *Adv. Phys.* **35** 375
[10] Tsuchiya M, Gaines J M, Yan R H, Simes R J, Holtz P O, Coldren L A and Petroff P M 1989 *Phys. Rev. Lett.* **62** 466
[11] Kapon E, Hwang D M and Bhat R 1989 *Phys. Rev. Lett.* **63** 430
[12] Ismail K, Antoniadis D A and Smith H I 1989 *Appl. Phys. Lett.* **54** 1130
[13] Jovanovic D and Leburton J P 1991 *Monte Carlo Device Simulation: Full Band and Beyond* ed K Hess (Dordrecht: Kluwer)
[14] Stroscio M, Kim K W and Littlejohn M A 1991 *Proc: SPIE* **1362** 566
[15] Sakaki H 1980 *Japan. J. Appl. Phys.* **19** L735
[16] Leburton J P, Briggs S and Jovanovic D 1990 *Superlatt. Microstruct.* **8** 209
[17] Manada T and Sone J 1989 *Phys. Rev.* B **40** 6265

[18] Briggs S, Jovanovic D and Leburton J P 1989 *Solid-State Electron.* **32** 1657
[19] Smith T P III, Arnot H, Hong J M, Knoedler C M, Laux S E and Schmid H 1987 *Phys. Rev. Lett.* **59** 2802
[20] Stormer H, Gossard A and Wiegenann W 1981 *Appl. Phys. Lett.* **39** 912
[21] Kim K W, Stroscio M A, Bhatt A, Mickevicius R and Mitin V V 1991 *J. Appl. Phys.* **70** 319
[22] Briggs S, Mason B and Leburton J P 1989 *Phys. Rev.* B **40** 12001
[23] Briggs S and Leburton J P 1988 *Phys. Rev.* B **38** 8163
[24] Matulionis A, Pozela J and Reklaitis A 1975 *Phys. Status Solidi* a **31** 83
[25] Brauer M 1977 *Phys. Status Solidi* b **81** 147
[26] Briggs S and Leburton J P 1989 *Superlatt. Microstruct.* **5** 145
[27] Jovanovic D, Briggs S and Leburton J P 1990 *Phys. Rev.* B **42** 11108
[28] Briggs S, Jovanovic D and Leburton J P 1989 *Appl. Phys. Lett.* **52** 2012
[29] Borenstain S I and Katz J 1989 *Appl. Phys. Lett.* **55** 654
[30] Colas E, Kapon E, Simhony S, Cox H M, Bhat R, Kash K and Lin P S D 1989 *Appl. Phys. Lett.* **55** 867
[31] Briggs S and Leburton J P 1991 *Phys. Rev.* B **43** 4785